



# Electrodynamic response study on railgun launcher based on electromechanical coupling model

Hong-cheng Xiao, Dong-mei Yin, Bao-ming Li\*

National Key Laboratory of Transient Physics, Nanjing University of Science and Technology, Nanjing, 210094, China



## ARTICLE INFO

### Article history:

Received 18 February 2019

Received in revised form

15 May 2019

Accepted 30 May 2019

Available online 3 June 2019

### Keywords:

Railgun launcher

Sliding contact

Dynamic properties

Elastic response

## ABSTRACT

The electrodynamic behavior of a medium caliber railgun launcher has been studied based on an electromechanical coupling model, which uses a unified modeling method for both electromagnetic and electromechanical field. This model adopts a material equivalent method to simulating the sliding contact behavior for the in-bore armature. An embedded node encoding program during field meshing operation provides good load transfer accuracy between electromagnetic field and mechanical field. Dynamic properties of in-bore magnetic field are firstly simulated and a subsequent dynamic analysis is conducted by mapping element results from electromagnetic analysis step to structure analysis step. The electromechanical-elastic response of the barrel is studied under the excitation current. The numerical model has shown reliability compared to experimental results.

© 2019 The Authors. Production and hosting by Elsevier B.V. on behalf of China Ordnance Society. This is an open access article under the CC BY-NC-ND license (<http://creativecommons.org/licenses/by-nc-nd/4.0/>).

## 1. Introduction

Since the understanding on the launch dynamic model of the railgun is not clear enough, some theoretical problems remain to be solved before its tactical application [1–5]. In the paper, the electrodynamic behavior of a medium caliber railgun launcher has been studied based on the electromechanical coupling model. The coupling model uses unified nonlinear finite element analysis (FEA) files for both electromagnetic and electromechanical analysis. An artificial encoding program on the numbering of the node and element is embedded in the numerical model during its physics field meshing progress. The ordered node encoding rule during FEA operation provides good accuracy for load transfer between electromagnetic field and mechanical field during electromechanical response calculation. The prepared 3-D electromagnetic and mechanical physics files will be simulated in the low frequency electromagnetic module and nonlinear mechanical module. Dynamic distributions of the magnetic field are firstly simulated and a subsequent mechanical analysis under the same time step will be conducted after mapping element results from electromagnetic

analysis step to structure analysis step, seeing Fig. 1. The quasi ballistic process of armature in bore is simulated by a synchronized iterative computing in each step. The sliding contact status can be estimated during iteration and a new rail-armature contact relation will be created in the next analysis step. The electrodynamic response of the barrel can be analyzed after iterations are finished for the whole launch process.

## 2. Electromechanical coupling model and the analysis procedure

### 2.1. Construction of quasi sliding contact model for rail-armature interaction

This model adopts a material equivalent method to simulating the sliding contact behavior between the rail and armature. The moving region of in-bore armature is created as a band before simulation. This region is set as air domain in advance and has a fine contact with the rails at initial launch time, seeing Fig. 2. With the predicted value of in-bore armature position at the specific time step, the armature geometry will be reconstructed by accurately selecting out the element entity in the space occupied by present armature material in the moving region. The attributes of the selected elements constructing the armature geometry are then modified and updated to the real armature attributes. For an accurate armature reconstruction in every analysis step, the armature

\* Corresponding author.

E-mail addresses: [hongcheng19901228@163.com](mailto:hongcheng19901228@163.com) (H.-c. Xiao), [baomingli@vip.sina.com](mailto:baomingli@vip.sina.com) (B.-m. Li).

Peer review under responsibility of China Ordnance Society

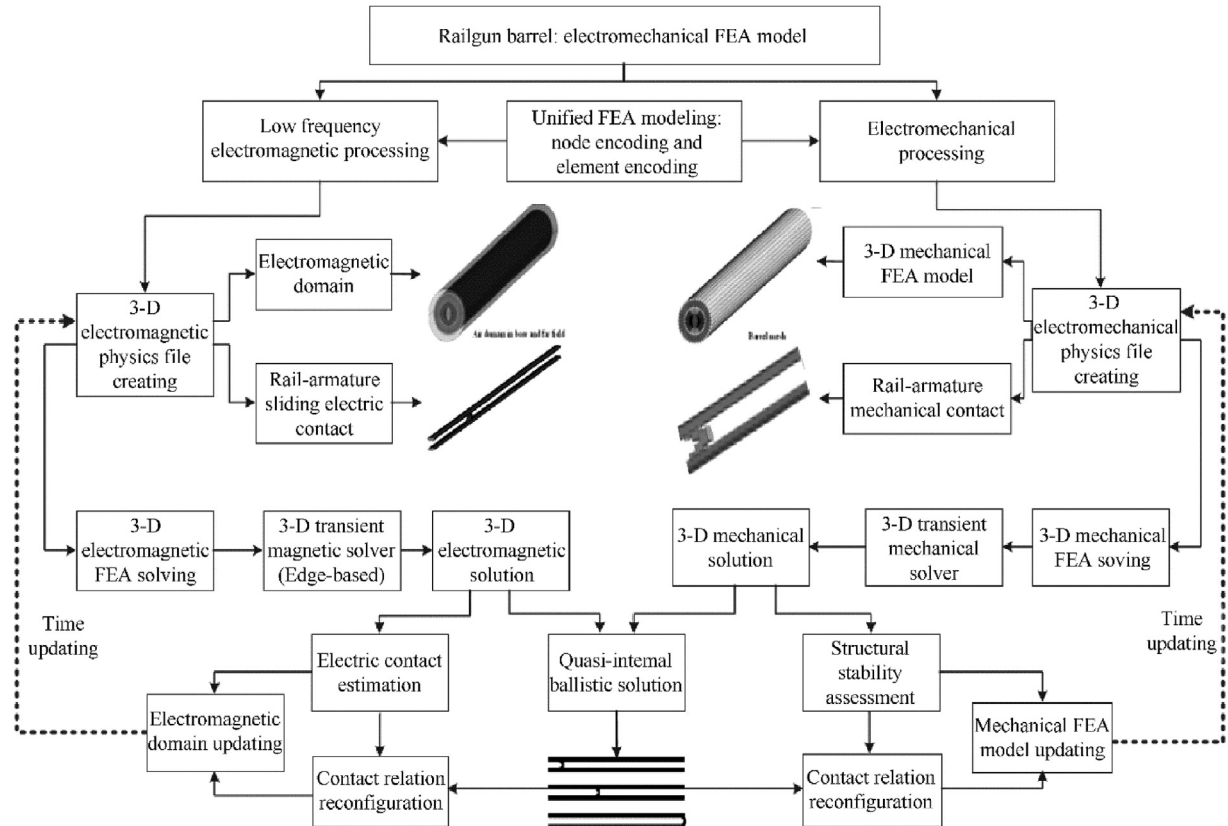


Fig. 1. Electromechanical FEA model.

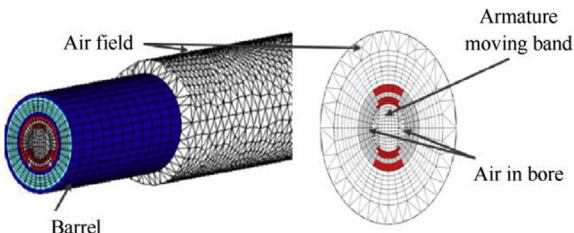


Fig. 2. Air domain around the barrel.

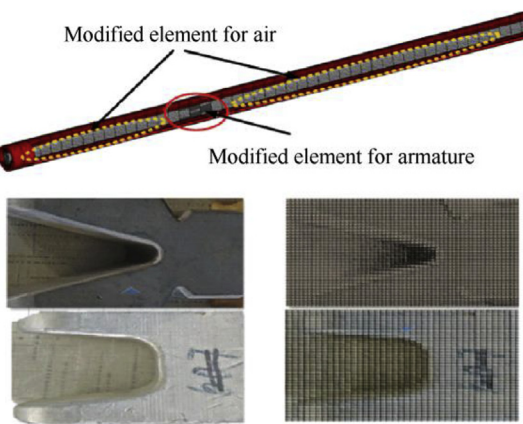


Fig. 3. Armature element configuration.

moving area is finely meshed and the nodes of the elements are artificially coded, which can be helpful for element selecting during armature reconstruction, seeing Fig. 3.

After the rail-armature contact and air domain are well defined, the FEA physics file will be extracted and submitted to transient electromagnetic analysis module for current density and flux density simulation. In every simulation step, the results from electromagnetic analysis will be extracted and loaded into an external subroutine of interior ballistics calculation. This subroutine systematically analyzes the acceleration history of the armature in bore and gives a prediction of armature position in the next analysis step, which will be adopted for rail-armature interaction redefinition and model updating in the next electromagnetic analysis step. After synchronizing all time steps in the electromagnetic and electromechanical FEA files, the analysis results in every time step will be shared between electromagnetic and electromechanical modules. In addition, the new rail-armature contact relation will be estimated in every analysis step. The estimation is a multiple-parameter diagnosis which involves contact load, contact stiffness, film thickness of discrete lubrication and other factors. Estimation results on rail-armature contact status in previous step will be used as the initial status for the next electromagnetic and electromechanical analysis step. The electromechanical-elastic response of the barrel can be acquired by the above time discrete analysis program after discharging current wave from pulse forming network (PFN) is tested during railgun shot.

## 2.2. Acceleration performance prediction of the launcher

This study systematically analyzes the acceleration history of the in-bore armature and acceleration performance of the launcher is

predicted mainly by the following steps [6]:

- (1) Assume the location, velocity and acceleration of armature at present  $t^i$  time step, are known as  $z^i$ ,  $\dot{z}^i$ ,  $\ddot{z}^i$ . Conduct one electromechanical analysis step at present time step with above FEA model and extract the armature driving force  $f_d^i$ , normal contact stress  $f_n^i$ ;
- (2) Calculate the acceleration value of the armature,  $\ddot{z}^{i+1}$  for next  $i + 1$  time,  $\ddot{z}^{i+1} = F^{i+1}/m$ ,  $F^{i+1} = f_d^i - F_f^{i+1} - F_a^{i+1}$ .  $F_f^{i+1}$  is the rail-armature friction force and  $F_a^{i+1}$  is aerodynamic drag of the armature.
- (3) Compute the velocity value of the armature,  $\dot{z}^{i+1}$  for next  $i + 1$  time,  $\dot{z}^{i+1} = \dot{z}^i + (\ddot{z}^i + \ddot{z}^{i+1})\frac{\Delta t}{2}$ ,  $\Delta t = t^{i+1} - t^i$ ;
- (4) Compute the displacement value of the armature,  $z^{i+1}$  for  $i + 1$  time,  $z^{i+1} = z^i + \dot{z}^i \Delta t + \left(\frac{1}{2} - \beta\right)\ddot{z}^i (\Delta t)^2 + \beta\ddot{z}^{i+1} (\Delta t)^2$
- (5) Substitute  $\ddot{z}^{i+1}$ ,  $\dot{z}^{i+1}$ ,  $z^{i+1}$  to FEA system to modifying and updating rail-armature contact zone. Repeat steps (1) through (5) until armature reaches the muzzle.

The rail-armature interaction during railgun shot includes tangent friction and normal contact force, seeing Fig. 4. The rail-armature friction force during a shot can be estimated as the following equation,

$$F_f = \begin{cases} f_e, & p = 0 \\ \mu_s f_n, & p = 0 \\ \mu_c f_n, & 0 < p \leq p_1, \\ (\mu_c \mu_v p) f_n, & p_1 < p \leq p_2, \\ (\mu_c p \mu_v) f_n, & p_2 < p, \end{cases} \quad \begin{array}{l} f_e \leq f_s \\ f_e > f_s \\ f_e > f_s \\ f_e > f_s \\ f_e > f_s \end{array}$$

Where,  $f_e$  refers to the external drive force on the armature.  $f_n$  is the normal stress on the rail-armature contact surface,  $f_s$  is the maximum steady-state friction force.  $p$  is a ratio coefficient relating to rail-armature friction power.  $p_1$  and  $p_2$  are the key values representing lubrication level. The friction coefficient used in the study is simplified to a function of rail-armature friction power [7], seeing following Fig. 5.

### 2.3. Program implementation based on FEA code development

A visual finite element analysis (FEA) platform by C# code design language, combined with Ansys computing core has been developed to design a graphical program “Emag\_launcher.exe”, for the electromechanical coupling analysis on the railgun barrel. Ansys provides effective field calculation for different physical environments. The sliding contact process and ballistic parameter calculation process are developed separately as subroutines and will be repeatedly called by the designed C# main interface. The most important feature of this code includes transient magnetic field calculation, rail-armature coupling mechanics and internal ballistic calculation. The main program includes a pre-processing unit for multi-parameters recording and physics files forming, a FEA solver unit for parametric model analysis and optimization. The

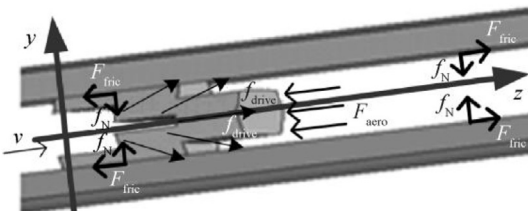


Fig. 4. Force diagram of rail-armature interaction.

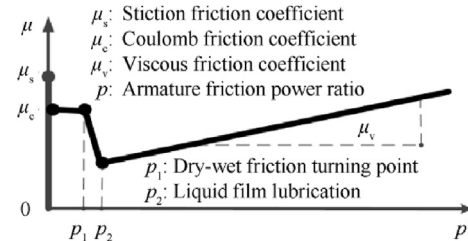


Fig. 5. Rail-armature friction mode.

simulation unit mainly includes electromagnetic module, electro-mechanical module and electro-thermal analysis module. In the post-processing unit, the results data document is processed to realize visualization and digital railgun simulation, seeing Fig. 6. This code provides the basis for the fast electromechanical analysis on the composite railgun barrel.

## 3. Electromagnetic analysis on an augmented railgun barrel

### 3.1. Electromagnetic field distribution on the composite barrel

A medium caliber railgun launcher is analyzed in the study. The barrel of the launcher has a 45 mm caliber and double turn rails in the bore. The rails and side wall are tightly packaged into glass fiber and T800 fiber wraps. The elliptical contour of bore and external package are shown in Fig. 7. The discharging current from PFN is a pulse which has a megampere amplitude and a millisecond duration, seeing Fig. 8. The current density on the main rail are solved by the program and distributions at 1.80 ms and 2.60 ms are shown in Fig. 9. The maximum current density generates in the back of the armature and the inner face of the main rail, which shows skin effect leads to energy concentration along the internal contour of the bore [8]. The magnetic flux density distribution in the longitudinal section of the barrel is shown in Fig. 9. Magnetic induction at present current level is about 24 T for double turn structure and no flux propagates into the external wraps of the composite barrel, as shown in Fig. 9. The magnetic flux density remains about 3T near the outer layers of the carbon fiber, but this value decreased to 0.02 T in the outer glass fiber layer.

### 3.2. Electromagnetic properties estimation of the launcher

The structure characteristic of the rail-armature circuit is shown in Fig. 10. The breech circuit contains two loops, including Turn 1 and Turn 2 in the figure. The muzzle circuit contains a Turn 3 loop. The electromagnetic properties of the augmented railgun launcher are estimated by the post processing part of the FEA platform. Two discharging pluses are analyzed in this part. Discharging current\_1 is 1120 kA with a 4.2 ms duration. Discharging current\_2 is 960 kA with a 5.1 ms duration, shown in Fig. 11. The driving force history on the armature has been calculated by the FEA code. The maximum propulsion on the armature is 529 kN by current\_1 and 422 kN by current\_2 respectively, as the curves shown in Fig. 11. Numerical simulation gives the transient voltage across the rail-armature circuit, which is induced by the circuit resistance under discharging excitation, as shown in Fig. 12. The breech voltage rises to kilovolt level due to strong skin effect and eddy current effect.

The total breech voltage and muzzle voltage under the transient field satisfy the following formulas,

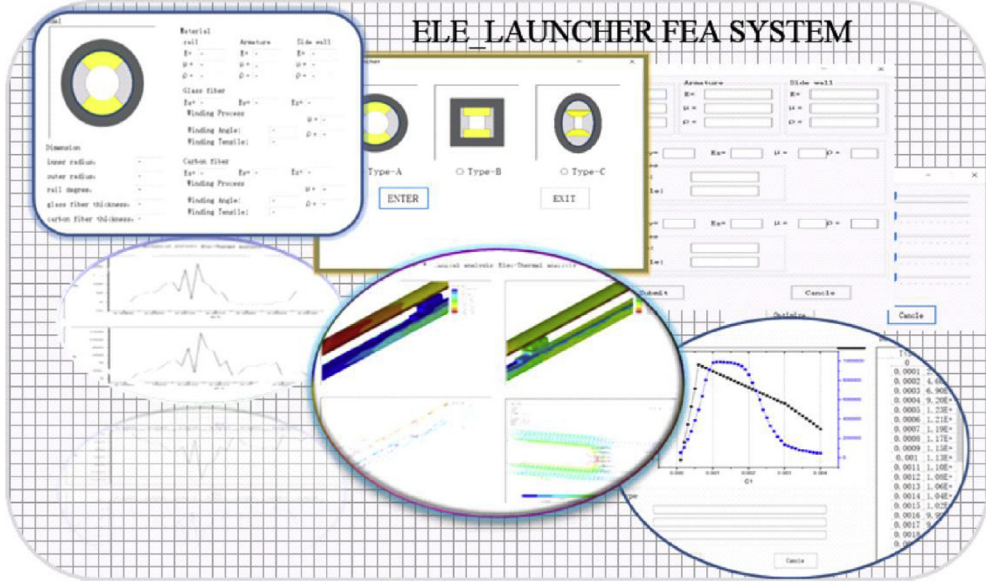


Fig. 6. Visual FEA platform for railgun barrel simulation.

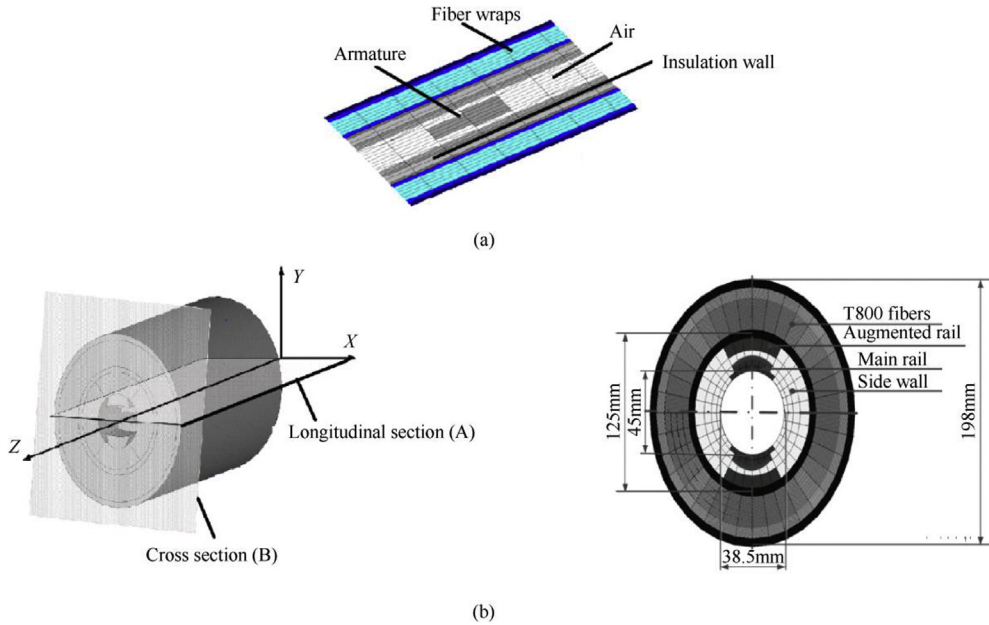


Fig. 7. Barrel structure of a 45 mm caliber, double turn railgun.

$$u_{bre} = u_{rb} + E_{bre} = i \cdot R_b + \frac{\Delta\varphi}{\Delta t_{turn1}} + \frac{\Delta\varphi}{\Delta t_{turn2}}$$

$$u_{muz} = u_{rm} + E_{muz} = i \cdot R_m + \frac{\Delta\varphi}{\Delta t_{turn3}}$$

Where,  $u_{bre}$  and  $u_{muz}$  are total voltages on the breech and the muzzle.  $u_{rb}$  and  $u_{rm}$  are resistance-voltages across the breech circuit and muzzle circuit.  $E_{bre}$  and  $E_{muz}$  are induced electromotive forces across the breech loop and muzzle loop. The total muzzle voltage is usually taken as a basis for judgment of rail-armature fine contact in previous studies [9–10]. So the FEA post processing part gives the computation of the total muzzle voltage. The back EMF in

Turn 3 is calculated as,

$$\frac{\Delta\varphi}{\Delta t_{turn3}} = \frac{\Delta(L \cdot i)}{\Delta t} = \frac{\Delta(L'x \cdot i)}{\Delta t} = L'i \frac{\Delta x}{\Delta t} + L'x \frac{\Delta i}{\Delta t}$$

Where,  $L$  is the inductance coefficient of Turn 3 circuit.  $L'$  is the inductance gradient along the rail length direction. The first item on the right of the equal sign can be modified as,

$$L'i \frac{\Delta x}{\Delta t} = BSv = B(l \cdot 1)v = Blv$$

Where,  $S$  is the area of Turn 3 loop with a unit length in rail length direction.  $l$  is the spacing between the inner rails. This infers that the back EMF on the muzzle is a superposition of two parts.  $L'i \frac{\Delta x}{\Delta t}$  is

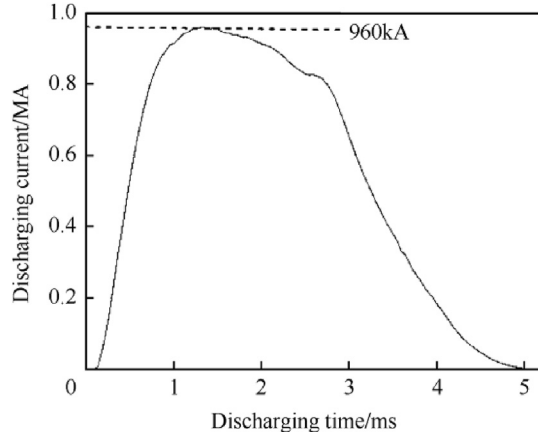


Fig. 8. Discharging current.

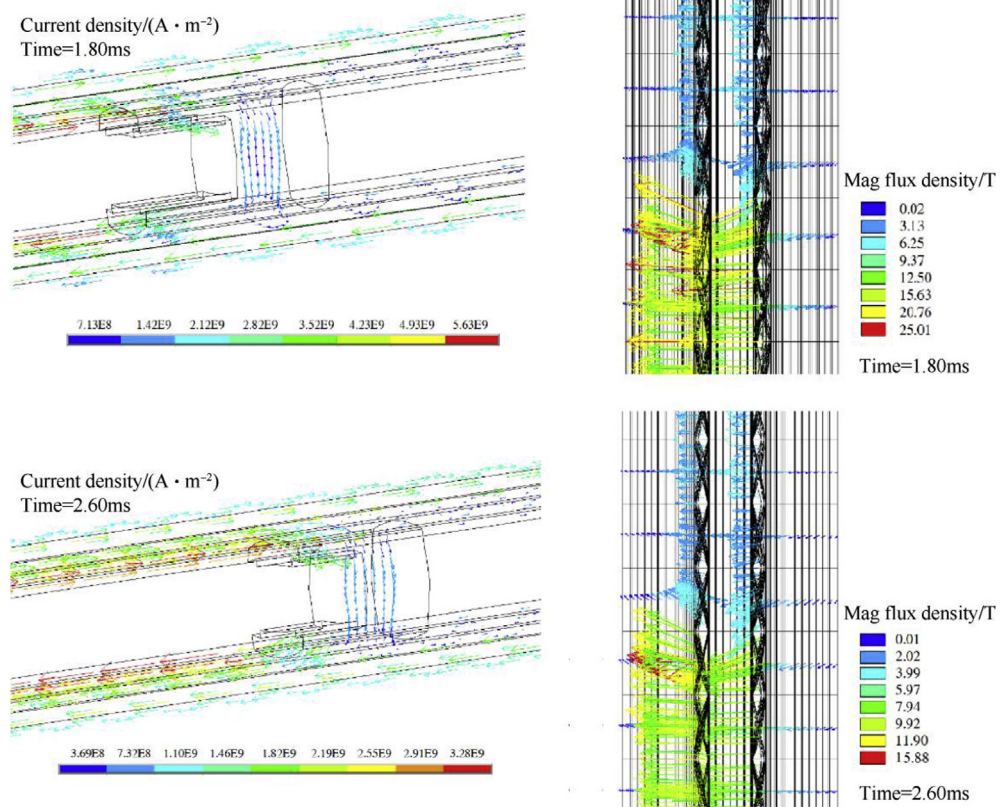


Fig. 9. Current density and magnetic flux density in the contact zone (in the longitudinal section, time = 1.80 ms, 2.60 ms).

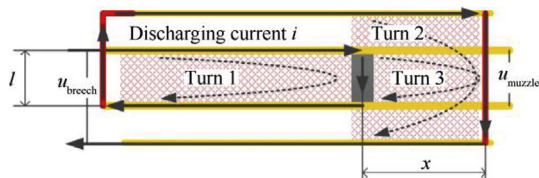


Fig. 10. Structure characteristic of the rail-armature circuit.

the motional electromotive force and  $L'x \frac{\Delta i}{\Delta t}$  is the induced electromotive force. The total muzzle voltages under discharging

current\_1 and current\_2 have been calculated and illustrated in Fig. 13 based on the superposition of above two voltage components.

The acceleration performance of the rail launcher has been studied by the coupled subroutine of interior ballistics calculation. In the interior ballistics process, the time-varying power and energy integral of the armature, total power and energy injected to the launcher are computed respectively. The efficiency of the rail launcher can be expressed as the following [11],

$$\eta = \frac{E_k}{E_{\text{inj}}}$$

The launching efficiency of the barrel is 18.9% under discharging current\_1 and 21.8% under discharging current\_2 by estimation, seeing Fig. 14. An optimized discharging current may improve the launching efficiency by reducing the residual electric energy after

projectile passes the muzzle by comparing the two current models. The acceleration performance of the barrel under above current excitations is shown in Fig. 15. 2201 m/s and 1970 m/s of armature velocities are achieved by excitation current\_1 and current\_2, which infers that higher peak current has better acceleration capability if overload in the railgun bore is well handled.

The double turn and half-double turn structure are analyzed here for magnetic improvement study [12]. As shown in Fig. 16. Type\_1 barrel has a 2.2-m-long augmented rail near the breech and type\_2 barrel has a full-size augmented rail. The magnetic flux density behind the armature is investigated under 1 MA excitation current. 24 T level of induction intensity is created by type\_2 barrel,

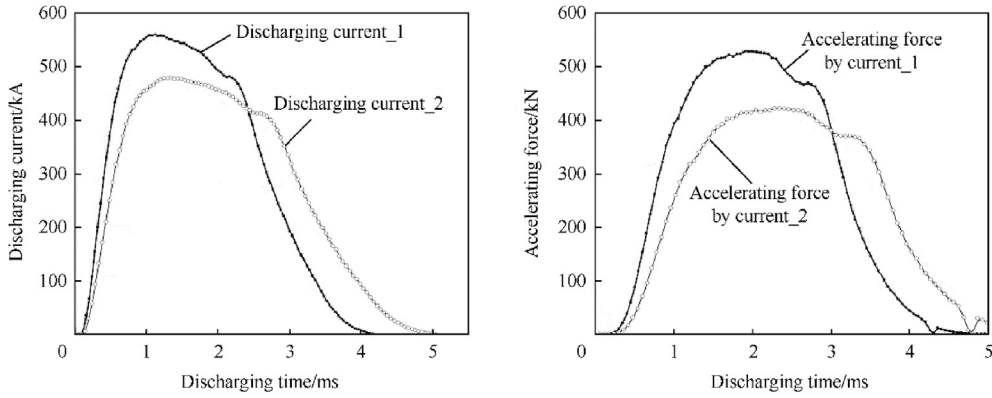


**Fig. 11.** Discharging pluses and electric propulsion histories.

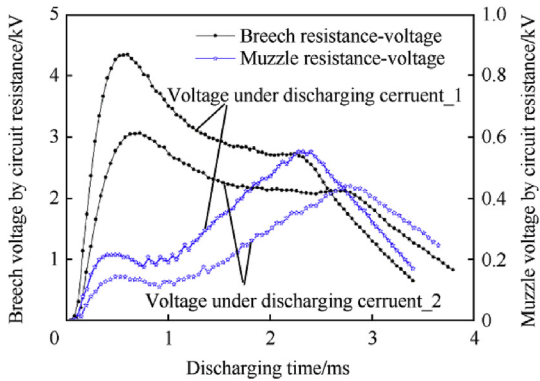


**Fig. 12.** Transient voltage across the rail-armature circuit.

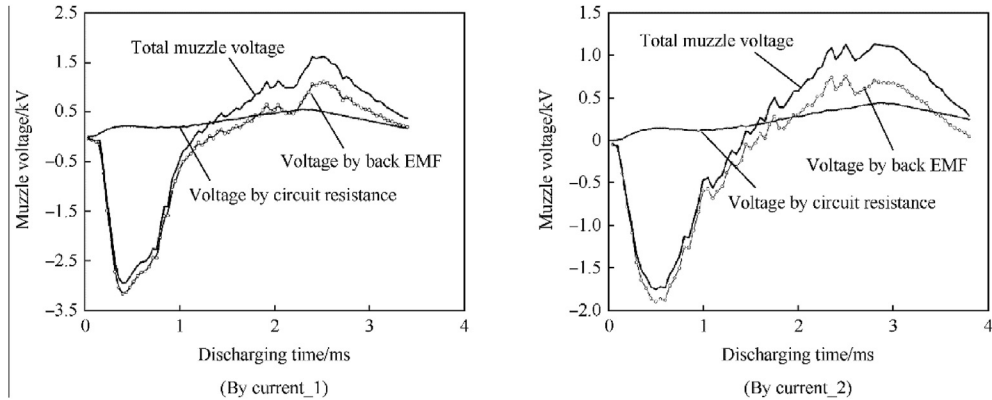


**Fig. 13.** Total muzzle voltage based on the superposition of two voltage components.

but the intensity is reduced to 7.5 T by typ\_1 barrel in its front half of the bore. The incremental inductance of the barrel is expressed by the following [13],

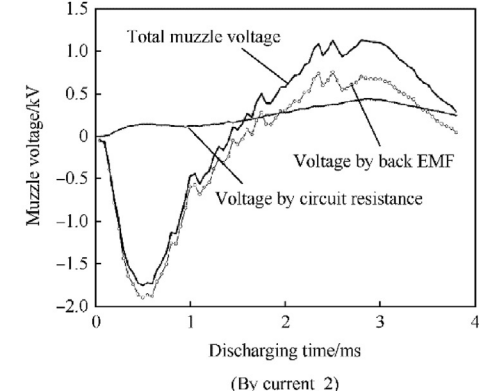
$$L = \frac{d\phi}{di}$$

Where,  $\phi$  is the transient flux in the railgun bore,  $i$  is the current flow through the rail-armature circuit. The inductance gradient of the barrel is derived as,

$$L' = \frac{L}{\int_0^t v dt}$$

The incremental inductance of the barrel during railgun shot is investigated and recorded in Fig. 17. The double turn structure has a 1.07  $\mu$ H/m inductance while a single turn structure has a 0.38  $\mu$ H/m inductance. The augmented rail has obvious effect on improving the transient in-bore flux, which is beneficial for armature acceleration.

### 3.3. Acceleration performance under different discharging current excitations



Further investigations on the acceleration capacity of the armature in bore have been conducted by the program [14]. Two groups of armature acceleration histories under different discharging pluses are analyzed. The first group is statistics on a 560 g of aluminum armature accelerated by current of 950–1100 kA. Another group is investigations on a 960 g of armature accelerated by excitation current of 1250–1550 kA, seeing Fig. 18. The interior ballistic process of armature in bore has been simulated and muzzle velocities of the armature under each excitation conditions are listed in Table 1. According to the numerical result, muzzle velocity of the armature will increase by about 20% with a full-size double turn barrel, compared to a half-augmented barrel. A high amplitude

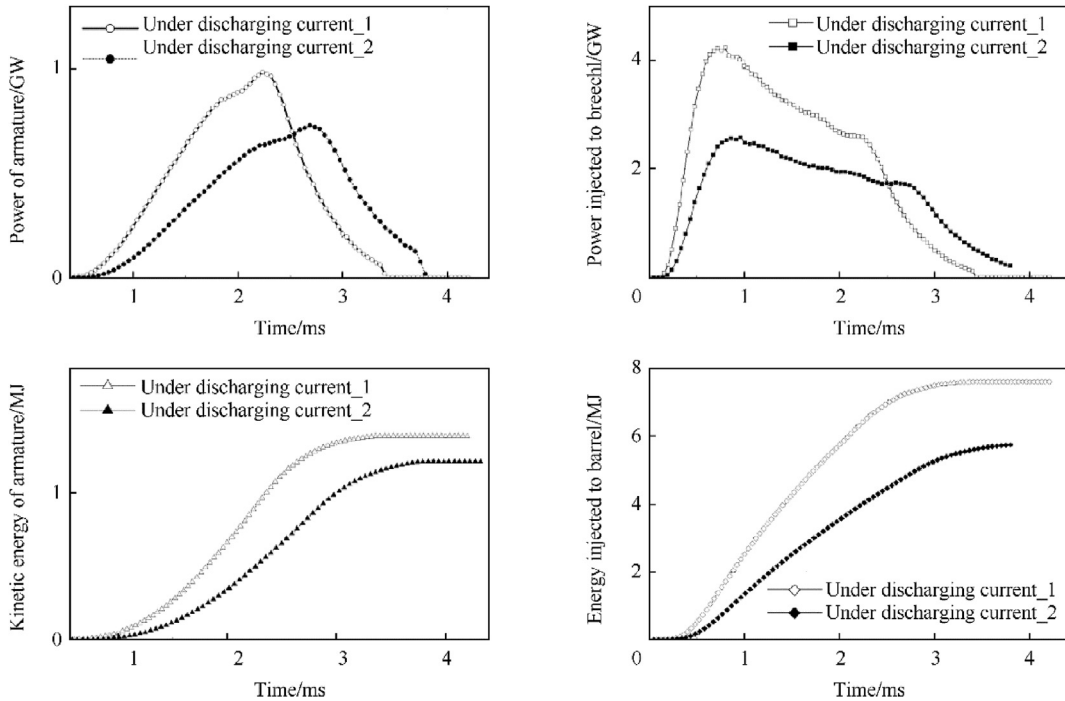


Fig. 14. Armature power vs. total power and armature kinetic energy vs. total energy.

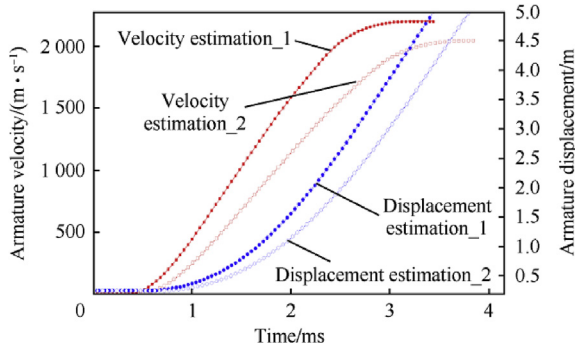


Fig. 15. Acceleration histories of the armature.

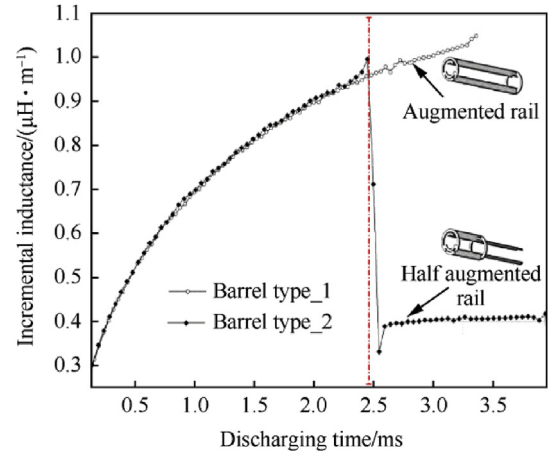


Fig. 17. Incremental inductance of type\_1 and type\_2 barrel during railgun shot.



Fig. 16. Diagram of augmented structure in type\_1 barrel and type\_2 barrel.

narrow pulse of discharging current will produce much better accelerating performance. And the length of the barrel in the electromagnetic launcher can be effectively shortened based on the effective length of its accelerating region.

#### 4. Forced response of the railgun barrel under electrodynamic force

The transverse vibration equation of fiber reinforced railgun barrel under time varying electrodynamic force can be estimated as the following [15]:

$$C^* I \frac{\partial^5 y}{\partial x^4 \partial t} + EI \frac{\partial^4 y}{\partial x^4} + c \frac{\partial y}{\partial t} + \rho A \frac{\partial^2 y}{\partial t^2} + ky = F_A + F_R \quad (1)$$

Where,  $C^*$  is damping coefficient related to the strain rate of the composite barrel.  $F_A$  is the force transferred from rail-armature dynamic contact.

$$F_A = \delta(x - \int v dt) \cdot f_n \quad (2)$$

Where,  $f_n$  is the normal contact force on the rail-armature interface.  $F_R$  is the time varying repulse force on the rail and can be expressed as,

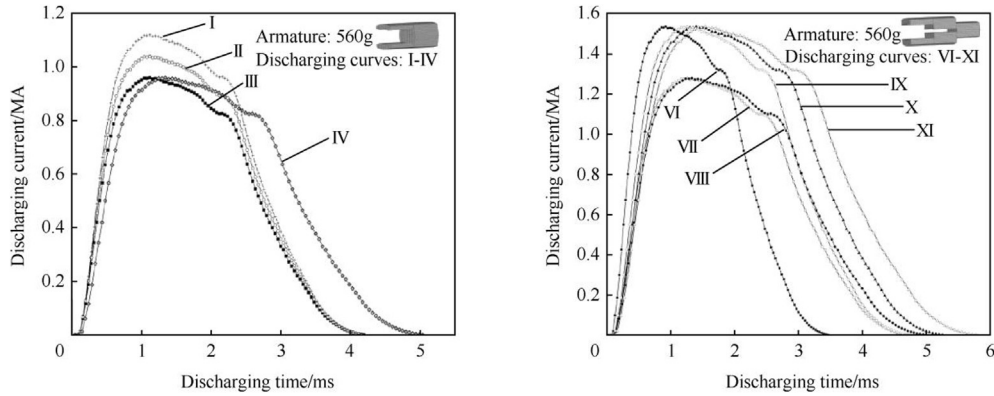


Fig. 18. Two groups of propulsion pluses for armatures.

**Table 1**  
Railgun acceleration performance with different rail and armature structures.

Armature	Rail	Current	Pulse duration/ms	Time in bore/ms	Accelerating time/ms	Accelerating region/m	Muzzle velocity/(m·s <sup>-1</sup> )
		I	4.20	3.44	3.20	4.38	2201
		IV	5.04	3.79	3.70	4.85	2046
		II	4.20	3.88	2.88	3.00	1979
		III	4.20	4.35	2.80	2.45	1465
		IV	5.04	4.20	3.45	3.68	1699
		VI	3.46	3.66	2.37	2.49	2288
		VII	4.72	4.27	3.42	3.16	1829
		IX	4.72	3.73	3.33	4.64	2626
		VIII	4.99	4.71	3.87	3.46	1995
		XI	5.25	3.65	3.25	4.73	3040
		VIII	4.99	4.90	3.04	2.45	1680
		VI	3.46	3.69	2.28	2.32	1929
		X	4.99	3.90	3.28	4.24	2283

$$F_R = q \cdot [1 - H(x - \int v dt)] \quad (3)$$

Where,  $q$  is the distributed repulse fore on the rail.  $H(x)$  is a step function. The armature is treated as a spring-quality-damper dynamic system and its impacting on the rail in the normal direction satisfies the following equation,

$$m \frac{\partial^2 u}{\partial t^2} + \bar{c} \frac{\partial e}{\partial t} + \bar{k} e = -mg$$

Where,  $u$  is the radial displacement of armature in the longitudinal

plane.  $\bar{c}$  is armature contact damping.  $\bar{k}$  is the normal contact stiffness between rail and armature.  $e$  is the relative displacement of rail-armature in the normal direction,

$$e = u - y$$

The normal contact face can be derived as,

$$f_n = \bar{k} e = -mg - m \frac{\partial^2 u}{\partial t^2} - \bar{c} \frac{\partial e}{\partial t} \quad (4)$$

Considered that the interference fitting between rail-armature is artificially constructed during the barrel assembling process,

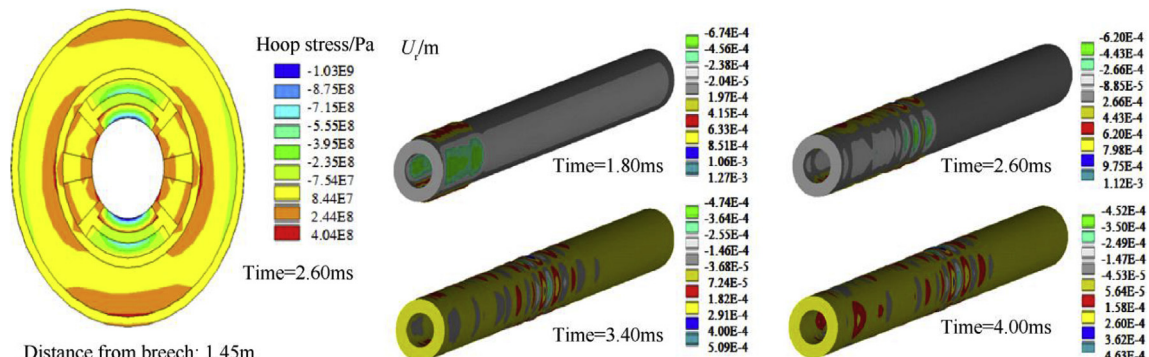


Fig. 19. Hoop stress in the cross section (time = 2.60 ms, peak current = 1120 kA) and radial deformation in the railgun bore (time = 1.8 ms, 2.6 ms, 3.4 ms and 4.0 ms).

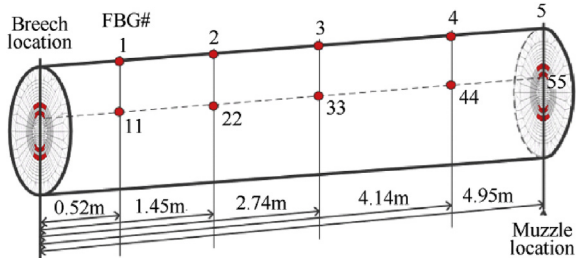


Fig. 20. Strain probe points on the augmented composite barrel.

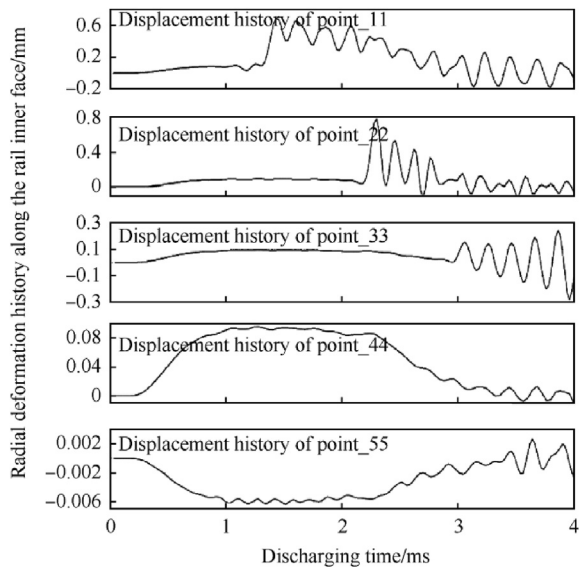


Fig. 21. Maximum radial deformation history on the bottom face of the main rail (peak current = 960 kA).

the radial displacement of armature  $u$  can be approximated as the following,

$$u = W(z) = W(\int v dt)$$

Where,  $W(z)$  is the interference on the rail-armature contact. The

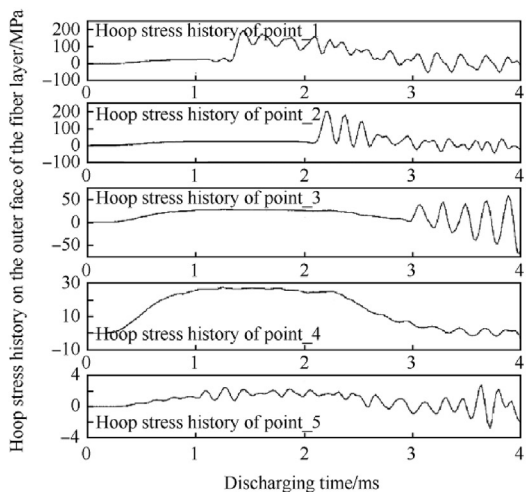
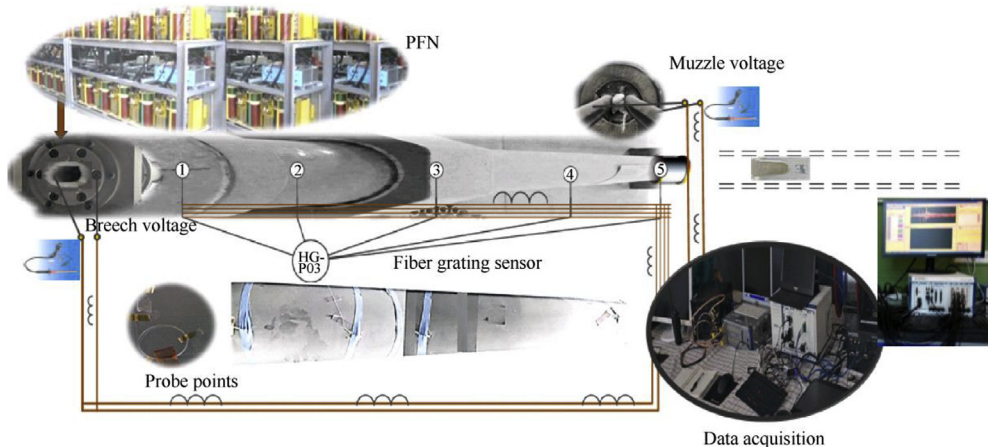


Fig. 22. Hoop stress history on the outer surface of the fiber layer and Mises stress history on the bottom surface of the main rail (peak current = 960 kA).

forced radial response of the railgun barrel during shot can be evaluated by the joint-solution of Eq. (1) to Eq. (4). In present study, the forced response of the barrel under electrodynamic force and rail-armature interference fitting force are simulated by the FEA system which is further developed based on Ansys software platform. The dynamic response of the 45 mm caliber barrel under 1120 kA excitation current is simulated. Fig. 19 shows the hoop stress distribution at 2.6 ms in the cross section which is 1.45 m from the breech during railgun shot. The maximum stress is about 1000 MPa appearing near the inner edge of the main rails as the skin effect produces serious current concentration here which results in serious stress concentration. The same thing happens to the augmented rails and about 720 MPa compressive stress exists in the inner edge of the rails. The maximum tensile stress on the rail-side wall interface is about 250 MPa. The radial deformation of the barrel, especially the outward expansion of the bore has significant effect on the rail-armature contact performance, which may lead transition if severe radial deformation happens in bore. The program conducts a survey on the transient radial deformation of the barrel based on real-time load transfer analysis. The radial deformation cloud diagrams of the barrel at four moments are listed in Fig. 19. Due to the non-uniform pressure in bore, the barrel has large radial expansion in the longitudinal cross section and obvious radial compression in the horizontal section. The maximum radial displacement of the rail at 1.80 ms reaches about 1.08 mm, which is located in the bottom surface of the main rail due to electromagnetic pressure and interference fit on the rail-armature contact [16–17].

The forced response of the barrel has been simulated with a discharging current of 960 kA injected into the main rail. Ten locations are selected as strain probe points which are evenly distributed on the inner surface of the rail and outer surface of the carbon fiber winding layers, as shown in Fig. 20 [18]. The time-varying deformation of the barrel at these probe points are shown in Fig. 21. The caliber of the barrel varies rapidly during launch. The maximum radial displacement on the main rail reaches about 0.7 mm near the breech. The hoop stress history in the outer surface of the fiber and Mises stress history in the bottom face of the rail are listed in Fig. 22. The stress histories in point\_33 and point\_44 show that a continuous pressure pulse exists in the front section of the barrel during the whole launch process. Due to the prolonged electromagnetic force in the whole augmented rail, the bore components may be weakened as the repulsive force is persistent in the barrel during launch. So, special considerations



**Fig. 23.** Experimental test arrangement on a 45 mm caliber augmented railgun (peak current = 1.2 MA, pulse duration = 4.1 ms, armature mass = 960 g).

should be given during the strength design and vibration design of the augmented railgun barrel.

## 5. Experimental tests

Experimental tests have been conducted on a 45 mm caliber augmented railgun barrel. The exciting current from the pulse power supply has a 1.25 MA peak value and 4.2 ms duration, seeing Fig. 24. Voltage distribution characteristic on the rail, stress characteristics in the fiber layer and muzzle velocity of the armature are also tested by the dynamic measurement system in the launching center, seeing Fig. 23. Accelerating history has been tested by probes and muzzle velocity of the armature reaches about 1875 m/s in the first group of 10 shots. Our simulation result is about 1993 m/s for this energy stage and the difference is currently attributed to

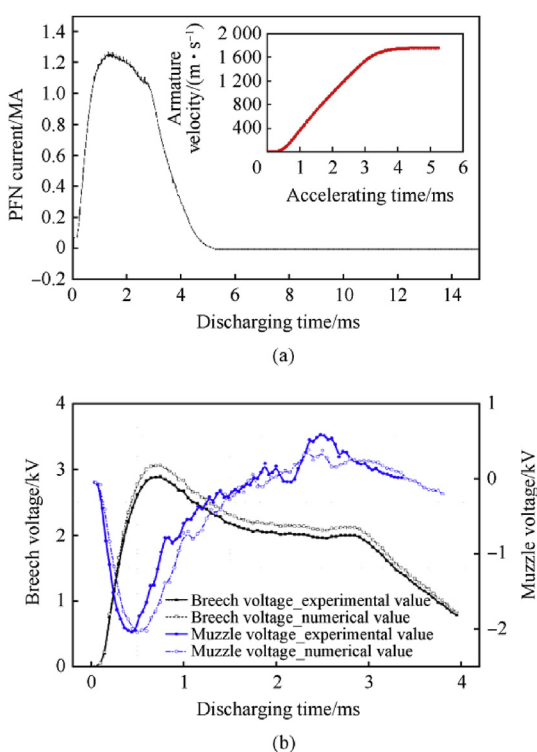


**Fig. 24.** (a) Current and armature velocity, (b) Voltage characteristic of the barrel.

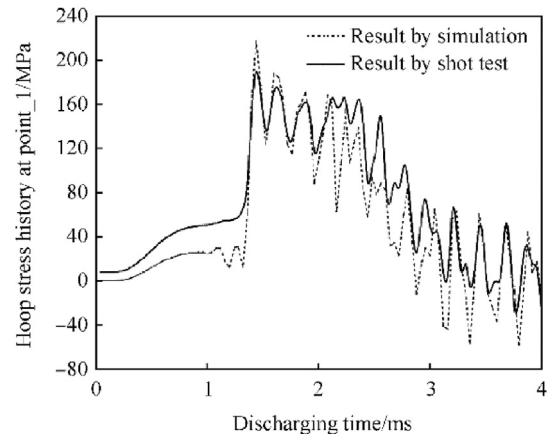


**Fig. 25.** Hoop stress-time history at point\_1.

the lack of cognitive on the internal ballistic process of in-bore armature.

The experimental breech voltage and muzzle voltage are acquired for comparing with the result from the numerical model, seeing Fig. 24. The dynamic hoop stress of the barrel is tested by fiber grating sensors which are installed on the outer surface of the fiber layer. Comparison on the experimental and theoretical value of hoop stress at point\_22 has been given in Fig. 25. The electrodynamic model in presented study shows good reliability and precise according to the comparative analysis between the experimental and numerical data.

## 6. Conclusions

The launch dynamics of a 45 mm caliber railgun launcher has been analyzed based on the electromechanical coupling model. The augmented railgun launcher produces about 450 kN driving power on a half a kilo of aluminum armature at 1 MA current level. The inductance gradient of the full-length augmented railgun structure is 2.8 times more than the gradient value in the single-turn structure, as the calculated result is 1.07  $\mu\text{H/m}$  and 0.38  $\mu\text{H/m}$  for both of them. The augmented type has about 20% launch efficiency and this is considered to be a normal performance compared to other rectangular-bore high inductance railgun. The exciting current caused stress concentration on the rail surface. 1 MA peak current produces near 1 GPa equivalent stress on the innermost surface of

the main rail, which has taken up more residual strength of the copper rail and will induce fast wear damage progress. This infers that a better profile of bore contour is important and internal convex contour of rail might reduce stress amplitude here in the middle of the rail surface. The numerical model proposed in the study has shown reliability compared to experimental results in our shot tests. However, errors in the accelerating performance evaluation shows an in-depth understanding on the rail-armature contact behavior should be proposed, especially considering more about thermodynamics in rail-armature contact. The dynamic response of the augmented railgun may be special as two pairs of vibration barrels exist in the bore and it should be further examined before its tactical application.

## References

- [1] Li BM, Lin QH. Analysis and discussion on launching mechanism and tactical electromagnetic railgun technology. *Def Technol* 2018;14(5):484–95.
- [2] Lehmann P, Vo MD, Wenning W. Comparative study of railgun housings made of modern fiber wound materials, ceramic, or insulated steel plates. *IEEE Trans Magn* 2005;41(1):200–5.
- [3] Wu JG, Tang B, Lin QH, et al. 3D numerical simulation and analysis of railgun gouging mechanism. *Def Technol* 2016;12(2):90–5.
- [4] Lou YT, Li HY, Li BM. Research on proximity effect of electromagnetic railgun. *Def Technol* 2016;123:223–6.
- [5] Lin QH, Li BM. Numerical simulation of interior ballistic process of railgun based on the multi-field coupled model. *Def Technol* 2016;12(2):101–5.
- [6] Westine PS. Prediction of transient displacement, velocity, and force on projectiles penetrating cohesive soils. *J Terramechanics* 1975;12(3):149–70.
- [7] Thomsen JJ, Fidlin A. Analytical approximations for stick-slip vibration amplitudes. *Int J Non-Linear Mech* 2003;38(3):389–403.
- [8] Ferrero R, Marracci M, Tellini B. Characterization of Inductance gradient and current distribution in electromagnetic launchers. *IEEE Trans Instrum Meas* 2011;60(5):1795–801.
- [9] Engel TG, Rada NM. Time- and frequency-domain characterization of railgun sliding contact noise. *IEEE Trans Plasma Sci* 2017;45(7):1321–6.
- [10] Li J, Cao B, Fan Z, et al. Judging the abnormal rail-armature contact states with waveforms of B-dot probes. *IEEE Trans Plasma Sci* 2017;45(7):1274–80.
- [11] Tian ZG, Meng XY, An XY, et al. Dynamic response of composite rail during launch process of electromagnetic railgun. *Acta Armamentarii* 2017;38(4):651–7.
- [12] Gallant J, Vanderbeke E, Alouahabi F, et al. Design Considerations for an electromagnetic railgun to be used against antiship missiles. *IEEE Trans Plasma Sci* 2013;41(10):2800–4.
- [13] Keshtkar A, Jafari Khorrami Z, Gharib L. Comparison of inductance gradient and electromagnetic force in two types of railguns with two projectiles by finite-element method. *IEEE Trans Plasma Sci* 2017;45(8):2387–92.
- [14] Hundertmark S, Schneider M, Vincent G. Payload acceleration using a 10 MJ DES railgun. In: Presented at the 16th international symposium on electromagnetic launch technology. May 15–19, 2012; 2012.
- [15] Su ZT, Xu D, Li XW, et al. Element time-history analysis for dynamic response of small-caliber guns with projectile-barrel coupling. *J Vib Shock* 2012;31(23):104–8.
- [16] Tzeng JT, Sun W. Dynamic response of cantilevered rail guns attributed to projectile/gun interaction—theory. *IEEE Trans Magn* 2007;43(1):207–13.
- [17] Tzeng JT, Hsieh KT. Electromagnetic field effect and analysis of composite structure. *IEEE Trans Plasma Sci* 2015;43(5):1536–40.
- [18] Gu JL, Luo HE, Qiang KJ, et al. Application of differential interference in electromagnetic rail gun strain measurement. *Appl Mech Mater* 2012;6:241–4.